Available online at www.sciencedirect.com
SCIENCE DIRECT
International Journal of Heat and Mass Transfer 49 (2006) 1501–1515
International Journal of HEAT and MASS TRANSFER
www.elsevier.com/locate/ijhmt

A numerical study of unidirectional solidification of a binary metal alloy under influence of a rotating magnetic field

P.A. Nikrityuk *, K. Eckert, R. Grundmann

Institute for Aerospace Engineering, Dresden University of Technology, Mommsenstrasse 13, D-01062 Dresden, Germany

Received 8 April 2005; received in revised form 18 August 2005
Available online 7 December 2005

Abstract

In this paper we present a numerical study of the fluid flow during directional solidification of a binary alloy (Pb85wt%Sn) in presence of a forced convection. The latter is driven by a rotating magnetic field (RMF) the strength of which, expressed by the magnetic Taylor number, varies between $10^4 < Ta < 2 \times 10^6$. The focus of this paper is the problem when cooling starts simultaneously with the acceleration of the melt from a state of rest. Thus, we study the interference of the so-called spin-up problem with the solidification of the melt. The numerical simulations are based on a mixture model formulation. We show that three distinct fluid flow phases exist. During the first two phases (*initial adjustment* and *inertial* phase) the acceleration of the liquid takes place which occurs in close similarity to the isothermal spin-up [P.A. Nikrityuk, M. Ungarish, K. Eckert, R. Grundmann, Spin-up of a liquid metal flow driven by a rotating magnetic field in a finite cylinder. A numerical and analytical study, Phys. Fluids 17 (2005) 067101]. The third phase is characterized by a braking of the fluid flow due to the progressive solidification increasing the aspect ratio of the liquid ($2R_0/H_l$) and decreasing the forcing. We show that as soon as the velocity of the secondary flow exceeds the velocity of the solidification front, a convex shape of the mushy zone can be observed. In parallel, Taylor–Görtler vortices advected by the secondary flow towards the mushy zone might impose a wavy substructure on the latter. At the end, predictions with respect to heat flux and macrosegregations are given.

Keywords: Solidification; Rotating magnetic field; Taylor–Görtler vortices; Spin-up

1. Introduction

Rotating magnetic fields are widely used in the metallurgical industry to eliminate flow asymmetries and to control heat and mass transfer toward the solidification front [1,2]. This effect is based on the swirling flow that homogenizes the liquid phase by suppressing thermosolutal convection and shrinkage-driven flow. Furthermore an important potential of RMFs lies in the ability to promote the columnar-to-equiaxed transition (CET) [3–5].

A rotating magnetic field (RMF) of angular frequency ω, applied to a liquid metal, drives a swirling flow by virtue of the azimuthal Lorentz force induced. If the liquid is confined in a cylinder of finite length, H_0, a secondary flow in the meridional plane appears, resulting from the imbalance between centrifugal force and radial pressure gradient inside the horizontal boundary layers [2]. A recent study by the authors [7,6] showed that the development of the RMF-driven flows occurs on the spin-up time scale given by $t_{\text{spin-up}} = \frac{H_0}{\sqrt{\nu\Omega_{\text{ce}}}}$. On applying this knowledge of RMF-driven flows onto the directional solidification we must be aware of the following key issues. First, the RMF-driven flow requires a characteristic time, $t_{\text{spin-up}}$, to become hydrodynamically developed, which means that the inviscid core actually rotates only from this moment on with angular velocity Ω_{ce}. Whether this transient must be taken into account or not depends on the cooling rate and the instant of switching on the RMF. Second, with progressive solidification the driving force itself is modified. Third, the aspect ratio A (diameter divided by height), in which the forced

* Corresponding author. Tel.: +49 351 463 38092; fax: +49 351 463 38087.
E-mail address: nikrityuk@tfd.mw.tu-dresden.de (P.A. Nikrityuk).

0017-9310/$ - see front matter © 2005 Elsevier Ltd. All rights reserved.
doi:10.1016/j.ijheatmasstransfer.2005.08.035

Nomenclature

A	aspect ratio of the cylinder
B	magnetic induction
c_p	specific heat
C	mixture mass concentration of Sn
D	mass diffusion coefficient
f	mass fraction
g	gravity acceleration
h	enthalpy
U_θ	volume-averaged azimuthal velocity
U_{rz}	volume-averaged meridional velocity
F_L	Lorentz force
Ha	Hartmann number
Ta	magnetic Taylor number
Fr	Froude number
Gr	Grashof number
E	Ekman number
H_0	height of cylinder
R_0	radius of cylinder
r, θ, z	cylindrical coordinate axes
$\vec{u}$	velocity
L	latent heat
p	pressure
p_B	the ratio of the number of poles to the number of phases in the current source
T	temperature
T_e	eutectic temperature
t	time
Re_ω	Reynolds number corresponding to the magnetic field rotation

Greek symbols

Ω	angular velocity
λ	thermal conductivity
σ	electric conductivity
μ	dynamic viscosity
ρ	density
β_S	solutal expansion coefficient
β_T	thermal expansion coefficient
ε	volume fraction of the liquid
ϑ	frequency of the alternating current
ν	kinematic viscosity
ω	angular frequency of the magnetic field
$\bar{\omega}$	relative frequency of the magnetic field
μ_0	magnetic permeability of freespace
η	axial efficiency of the Lorentz force

Subscripts

e	eutectic
l	liquid phase
s	solid phase
m	mixture
ce	core effective
cr	critical
t	turbulence
ref	reference
0	initial value
w	wall

convection takes place is increased. The convection must adapt to this since the ratio of forcing Lorentz torque to the braking torques imposed from side walls and bottom is changed.

First insights into the flow structure during RMF-driven solidification came from numerical [3,9] and experimental [10] works. The experimental and computational study of an aluminum alloy A356 with a RMF solidification [3] showed, beside the promotion of the CET, a significant radial and axial segregation of silicon concentration and eutectic fraction. However, the details of the turbulent flow could not be measured and the algebraic turbulence model used in the numerical simulations was not able to capture flow instabilities such as Taylor–Görtler vortices. The RMF-driven directional solidification of binary AlSi7 alloy under microgravity conditions was numerically studied by Hainke et al. [9]. They showed that beyond a certain Ta number a liquid channel at the axis of the sample inside the mushy zone is formed which is responsible for the macrosegregations detected. These simulations are restricted to Ta numbers which are several orders of magnitude smaller than those used in technological applications of RMFs. First measurements of the velocity fields during solidification of PbSn alloys by Eckert et al. [10] show, at an advanced stage of solidification, that significant deviations occur from the symmetric double vortex structure known from the isothermal case.

To sum up, our understanding of the complex interactions between liquid, mush zone, solidification front and RMF-driven convection is far from being complete. All of the key issues addressed above still await detailed consideration. In particular, how relevant is the spin-up phase for the entire solidification? How does the RMF-driven flow modify the shape of the mush zone? To gain deeper insights into these questions we use the fluid dynamics code of [7,6] combined with a mixture model [11] model which is particularly suited to study the aspects of fluid flow during solidification. The model system considered in this study is a binary PbSn alloy (Pb85wt%Sn) solidified with a cooling rate for which the solidification time and $t_{\text{spin-up}}$ are comparable. In this paper we show for the first time important details about the development of the RMF-driven flow during solidification up to $Ta \sim \mathrm{O}(2 \times 10^6)$. Beside the identification of different flow phases we show the impact of the secondary flow which becomes noticeable as soon as its averaged velocity exceeds that of the solidification

front. Furthermore we analyze the influence of Taylor–Görtler vortices on the shape of the mushy zone.

The paper is organized as follows: in Section 2, the mixture model and the relationships needed for the closure of the energy and the species conservation equations are introduced. This section is completed with a description of the numerics and its validation. In Section 3 we analyze the flow dynamics in the case when spin-up of the melt and solidification interfere. To better understand the impact of gravity on the flow patterns observed in Section 3.3 we show simulations with vanishing gravitational acceleration. The macrosegregations resulting from the RMF-driven flow are studied in Section 3.4. The discussion in Section 4 is focused on a criterion for the *Ta* number beyond which the effect of buoyancy can be neglected. The results are summarized in Section 5.

2. Mathematical formulation of the problem

2.1. Rotating magnetic field

We consider a finite cylinder with radius R_0 and height H_0 filled with a liquid alloy. The rotating magnetic field initializes a Lorentz force, F_L, leading to the rotation of the liquid alloy. The induced F_L is composed of two parts: a mean axisymmetric component which is time-independent and a time-dependent one, oscillating with the double frequency. The latter one has a minor effect on the fluid flow [12] and is therefore not considered in this work. The interaction of a RMF with a conducting liquid depends on several dimensionless quantities: $Ha = BR_0\sqrt{\frac{\sigma}{2\mu}}$, $Re_\omega = \frac{\rho\omega R_0^2}{p_B\mu}$ and $\bar{\omega} = \mu_0\sigma\omega R_0^2$, where $\omega = 2\pi\vartheta$, and the aspect ratio $A = 2R_0/H_0$. *Ha* and Re_ω can be unified to the magnetic Taylor number $Ta = Ha^2 Re_\omega$.

In our case the RMF is of low frequency and low induction. The low-frequency case is justified due to $\bar{\omega} < 1$ leading to a skin depth $\left(\sqrt{\omega\sigma\mu_0}\right)^{-1}$ of approximately 5 cm which exceeds the radius of the mold we use ($R_0 = 2.5$ cm). The low-induction condition implies that the angular velocity induced by the RMF does not change the magnetic field applied. It is satisfied since $\frac{Ha^4}{Re_\omega} \ll 1$ [13]. With respect to PbSn alloy, geometry and RMF ($\vartheta = 50$ Hz, $p_B = 1$) we use the following values: $A = 0.79$, $\bar{\omega} = 0.471$, $Re_\omega = 8.15\times10^5$. The corresponding values of Taylor and Hartmann numbers are given in Table 1.

Once the low-frequency and low-conduction conditions are fulfilled, an analytical solution can be written for the time-averaged Lorentz force (in electroconductive homogeneous media), which has an azimuthal component (the meridional component of the Lorentz force has a minor effect on the fluid flow in comparison to the azimuthal component [13], thus we neglect it). It is a function of the position only and has the following shape [14]:

$$F_{L\theta} = \frac{1}{2}\sigma\cdot\omega\cdot B^2\cdot r \cdot\left(1-\frac{2}{r'}\sum_{k=1}^{\infty}\frac{J_1(\zeta_k r')\cdot\cosh\left(\zeta_k\left(z'-\frac{1}{2}H'\right)\right)}{\left(\zeta_k^2-1\right)\cdot J_1(\zeta_k)\cdot\cosh\left(\frac{1}{2}\zeta_k H'\right)}\right), \quad (1)$$

where $z' = z/R_0$, $r' = r/R_0$, $H' = H_0/R_0$, J_1 is Bessel function of the first kind, ζ_k are the roots of $J_1'(x) = 0$.

2.2. Assumptions

The continuum model [11] has been adopted for the binary alloy solidification under the following assumptions:

1. The differences in density and electric conductivity between solid and liquid phase are neglected.
2. The mushy region is modeled by means of using a mixture viscosity.
3. The phases are in local thermodynamic equilibrium. The phase diagram is applied.
4. The flow of the liquid phase is axisymmetric.
5. The solid and liquid phases are assumed to have the same velocity in the upper mushy zone ($\varepsilon > \varepsilon_{cr}$).

The last assumption follows from $\rho_l = \rho_s$ (assumption 1). As it was shown by Ni and Incropera [15] for equivalent phase densities it is reasonable to assume equivalent solid and liquid velocity components, see Eqs. (13) and (20) in Ref. [15]. Unfortunately we did not find in the literature theoretically predicted relationship between velocities of solid and liquid phases for the case of forced swirling liquid melt. Generally the assumption 5 corresponds to the limit case frequently used in the modeling of an equiaxed grain movement [16,17].

2.3. Governing equations

Based on the assumptions made above, the set of equations in Boussinesq approximation has the following form:

Mass conservation equation:

$$\frac{\partial\rho}{\partial t} + \nabla\cdot(\rho\vec{u}) = 0. \quad (2)$$

Table 1
The values of magnetic Taylor, Hartmann, Ekman numbers, core rotation rate and spin-up time corresponding to magnetic induction

B (mT)	Ta	Ha	E	Grid (CVr × CVz)	Δt (s)	Ω_{ce} (s^{-1})	$t_{spin\text{-}up}$ (s)
0.5	5.1×10^4	0.25	1.1×10^{-3}	50×120	0.025	0.32	228.9
1	2.04×10^5	0.5	4.4×10^{-4}	70×150	0.025	0.80	144.2
3	1.83×10^6	1.5	1.0×10^{-4}	100×260	0.02	3.48	69.3

The grids and time steps used by numerical simulations are included.

Momentum conservation equation:

$$\frac{\partial(\rho\vec{u})}{\partial t}+\nabla\cdot(\rho\vec{u}\cdot\vec{u})=-\nabla p+\nabla\cdot(\mu_{\mathrm{m}}\nabla\vec{u})+\rho\vec{g}(\beta_{\mathrm{T}}(T-T_{\mathrm{ref}})+\beta_{\mathrm{C}}(C-C_{\mathrm{ref}}))+\vec{F}_{\mathrm{L}}, \tag{3}$$

where T_{ref} and C_{ref} correspond to the initial temperature, $T_0=293$ °C, and the mixture mass concentration of Sn, $C_0=0.85$, of the molten alloy, respectively. The projection of the momentum conservation equation in azimuthal direction has the form:

$$\frac{\partial(\rho u_\theta)}{\partial t}+\nabla\cdot(\rho\vec{u}\cdot u_\theta)=\nabla\cdot(\mu_{\mathrm{m}}\nabla\vec{u})-\frac{\mu_{\mathrm{m}}u_\theta}{r^2}-\frac{\rho u_r u_\theta}{r}+F_{\mathrm{L}\theta}, \tag{4}$$

where the last term in the Eqs. (3) and (4) involves the Lorentz force, which has only an azimuthal component. The mixture viscosity is calculated by using the following approximation formula [3]:

$$\mu_{\mathrm{m}}=\begin{cases}\mu_{\mathrm{l}}\cdot e^{(4.5\cdot(1-\varepsilon))}, & \varepsilon\geqslant\varepsilon_{\mathrm{cr}},\\ b1\cdot(1-\varepsilon)+b2, & (\varepsilon_{\mathrm{cr}}-0.1)<\varepsilon<\varepsilon_{\mathrm{cr}},\\ \varepsilon\mu_{\mathrm{l}}+(1-\varepsilon)\mu_{\mathrm{s}}, & \varepsilon\leqslant(\varepsilon_{\mathrm{cr}}-0.1).\end{cases} \tag{5}$$

Note that in this work we use $\varepsilon_{\mathrm{cr}}=0.8$, instead of $\varepsilon_{\mathrm{s_{cr}}}=0.4$ as it was in [3]. The expressions (5) divide the mushy zone into two zones. The first one for which $\varepsilon\geqslant\varepsilon_{\mathrm{cr}}$ is a moderately viscous zone still allowing for fluid flow. The second zone ($\varepsilon<\varepsilon_{\mathrm{cr}}$) is a highly viscous one. The constants $b1$ and $b2$ in Eq. (5) were obtained from a linear interpolation between the points $(\varepsilon_{\mathrm{cr}}-0.1)$ and $\varepsilon_{\mathrm{cr}}$. The value of μ_{s} was set to 100 Pa s.

Energy conservation equation:

$$\frac{\partial(\rho h)}{\partial t}+\nabla\cdot(\rho\vec{u}\cdot h)=\nabla\cdot\left(\frac{\lambda}{c_{ps}}\nabla h\right)+\nabla\cdot\left(\frac{\lambda}{c_{ps}}\nabla(h_{\mathrm{s}}-h)\right)-S_{\mathrm{h}}. \tag{6}$$

Here S_{h} stands for the source term $\nabla\rho(\vec{u}-\vec{u_{\mathrm{s}}})\nabla(h_{\mathrm{l}}-h)$ which takes into account that $\vec{u}-\vec{u_{\mathrm{s}}}$ instead of $\vec{u}$ is the pertinent velocity by which latent heat is advected. Note that $S_{\mathrm{h}}=0$ when solid and liquid phases move with the same velocity.

The liquid and solid enthalpies are related to the equilibrium temperature through the following thermodynamic relations:

$$h_{\mathrm{l}}=c_{pl}T+(c_{ps}-c_{pl})T_{\mathrm{e}}+L\quad\text{and}\quad h_{\mathrm{s}}=c_{ps}T. \tag{7}$$

Species mass conservation equation:

$$\frac{\partial(\rho C)}{\partial t}+\nabla\cdot(\rho\vec{u}\cdot C)=\nabla\cdot(\rho D_{\mathrm{m}}\nabla C)+\nabla\cdot(\rho D_{\mathrm{m}}\nabla(C_{\mathrm{l}}-C))-S_{\mathrm{c}}. \tag{8}$$

Here $S_{\mathrm{c}}=\nabla\rho(\vec{u}-\vec{u_{\mathrm{s}}})\nabla(C_{\mathrm{l}}-C)$ is the source term governing the convective transport of solute rejected from the mushy zone. Again, $S_{\mathrm{c}}=0$ if there is no relative movement between liquid and solid.

Based on the assumption 1 the mixture quantities are defined in the following manner:

$$f_{\mathrm{l}}=\varepsilon,\quad f_{\mathrm{s}}=(1-\varepsilon), \tag{9}$$

$$h=f_{\mathrm{s}}h_{\mathrm{s}}+f_{\mathrm{l}}h_{\mathrm{l}},\quad C=f_{\mathrm{s}}C_{\mathrm{s}}+f_{\mathrm{l}}C_{\mathrm{l}}. \tag{10}$$

Material properties of the mixture, such as the thermal conductivity and the mass diffusion coefficient, are linear dependent on the volume fraction of liquid. Material properties of each alloy component were calculated from linear dependency on the mass concentration of its component. The material properties of pure Pb and Sn are listed in Table 2.

2.4. Closure of energy and species conservation equations

The closure of the system of conservation equations requires supplementary relationships between ε, h and C. With the assumption of local equilibrium, these expressions can be obtained from the equilibrium phase diagram [22]. The volume fraction of the liquid in the mushy zone is approximated by means of a conduction-dominated solidification rule:

$$\varepsilon=\left|\frac{T-T_{\mathrm{s}}}{T_{\mathrm{l}}-T_{\mathrm{s}}}\right|, \tag{11}$$

Table 2
The material properties of Pb and Sn

Symbol	Properties	Sn	Pb	References
L_{f}	Latent heat (J/kg)	59 600	23 200	[18]
T_{melt}	Melting temperature (°C)	231.9	327	[18]
c_{ps}	Specific heat of the solid phase (J/kg K)	226	125	[19]
c_{pl}	Specific heat of the liquid phase (J/kg K)	238	210	[19]
λ_{s}	Thermal conductivity of the solid phase (W/m K)	62	35.3	[19]
λ_{l}	Thermal conductivity of the liquid phase (W/m K)	28	16	[19]
ρ_{s}	Density of the solid phase (kg/m^3)	7280	11 340	[18]
ρ_{l}	Density of the liquid phase (kg/m^3)	7000	10 821	[20]
ρ	Average density (kg/m^3)	7140	11 085.5	
μ_{l}	Molecular viscosity of the liquid (N s/m^2)	1.78×10^{-3}	2.4×10^{-3}	[21]
D_{l}	Binary diffusion coefficient Sn in Pb for the liquid phase (m^2/s)	1.5×10^{-9}		[21]
D_{s}	Binary diffusion coefficient Sn in Pb for the solid phase (m^2/s)	1.5×10^{-12}		[21]

$\sigma=1.5\times10^6$ (A/V m).

where T_s and T_l are the temperatures on the solidus and liquidus line in the phase diagram. The functional dependencies of T_s and T_l, which were gained by approximation of the phase diagram [22] by means of the least square method have the following form:

$$T_l = \begin{cases} 327.05 - 338.39 \cdot C + 479.62 \cdot C^2 - 500.93 \cdot C^3, \\ \quad C \leqslant 0.619, \\ 101 + 134.9 \cdot C - 3.91 \cdot C^2, \\ \quad 0.619 < C < 1, \end{cases} \tag{12}$$

$$T_s = \begin{cases} 327.52 - 884.7 \cdot C + 7181.11 \cdot C^2 - 36\,339.5 \cdot C^3, \\ \quad C \leqslant 0.183, \\ 183\ ^\circ\mathrm{C}, \\ \quad 0.183 < C \leqslant 1. \end{cases} \tag{13}$$

An overview of existing algorithms for the closure problem is given in [23]. Most of the algorithms are based on the temperature-source energy equation, where the temperature is calculated directly from the energy equation. In this work we introduce an iterative procedure for the calculation of the volume fraction of liquid if the mixture enthalpy is the principle variable. In order to define the volume fraction of liquid from the given mixture enthalpy and mixture mass concentration at the given time, the set of Eqs. (7), (9), (10) and (11)–(13) is solved iteratively. This procedure is done for each nodal point of the grid and includes the following steps:

1. Calculate T_l and T_s from Eqs. (12) and (13) by using C gained from Eq. (8).
2. Calculate f_l, f_s and $L = L_{Sn} \cdot C_l + L_{Pb} \cdot (1 - C_l)$, where C_l is taken from phase diagram according current value of T.
3. Calculate $T^{i+1} = \frac{h - f_l \cdot [(c_{ps} - c_{pl}) \cdot T_e + L]}{c_{ps} f_s - c_{pl} f_l}$.
4. If $T^{i+1} \geqslant T_l$, so $\varepsilon = 1$, stop. $T^{i+1} \leqslant T_s$, so $\varepsilon = 0$, stop.
5. Calculate ε^{i+1} from Eq. (11). To avoid oscillations, arising from the volume fraction calculation on the liquid/mush- and solid/mush-boundaries, the following relaxation is used: $\varepsilon^{i+1} = (1 - \alpha_\varepsilon) \cdot \varepsilon^i + \alpha_\varepsilon \cdot \varepsilon^{i+1}$ where α_ε is the relaxation factor which was set equal to 0.5. ε^i is the liquid volume fraction from the previous iteration.
6. Check the convergence: If $|T^{i+1} - T^i| < 10^{-3}$, then stop; if not then $T^i = T^{i+1}$, $\varepsilon^i = \varepsilon^{i+1}$ go to 2.

2.5. Alloy composition, boundary conditions, numerical scheme and code validation

In this study we restrict ourselves to the hypereutectic alloy Pb85wt%Sn. When starting unidirectional solidification (UDS), Pb85wt%Sn shows an initially stable stratification with respect to both the thermal and the solutal density change. This is due to cooling from below and rejection of heavier Pb. Thus without forced convection, the UDS of Pb85wt%Sn-alloy is not affected by thermosolutal convection since shrinkage-driven flow is negligible. However, as soon as RMF-driven convection sets in, radial temperature and solute gradients can appear due to the secondary flow. Thus with advancing solidification buoyancy must be taken into account.

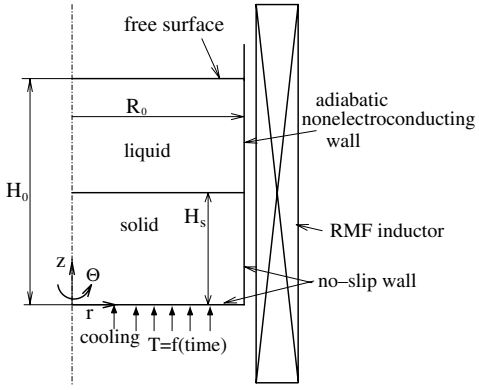

Fig. 1. Scheme of the calculated domain.

Fig. 1 sketches the domain used in the computations. The initial temperature was set to 293 °C according to the experiment [4]. To model the mold's bottom cooling we use a time-dependent Dirichlet boundary condition for the energy conservation equation in the form of the given temperature. The temperature values were taken from the experiment done by Willers et al. [4]. Namely the bottom temperature we used equals to the temperature measured by the nearest to the bottom thermoelement. According to the experiment [4] the time-averaged cooling rate corresponds to about $\mathrm{d}T/\mathrm{d}t = 1$ K/s. The top and side wall are adiabatic; all interfaces are impermeable to Pb and Sn. The bottom and the side wall are no-slip. The upper free surface is free of tangential stresses and non-deformable. Thus, we neglect both surface tension effects and the non-flatness of the interface due to the rotation. The first can be justified by the coverage of the liquid metal surface by an oxide film, which suppresses Marangoni stresses. The rotation of the liquid causes a deformation of the free surface proportional to the Froude number $Fr = \frac{\Omega^2 R^2}{gH}$ [24]. It was shown experimentally [24] that for $Fr < 0.1$ the free surface of rotating fluid can be treated as a flat surface. Thus, the latter is a good approximation for our work since the Froude number does not exceed 0.1 in this study. Applied to a RMF-driven flow with upper free surface this approach showed a reasonable agreement between experimental [25] and numerical data [7].

The solidification model described above has been implemented into the open source code of a 2D Navier–Stokes solver [26], where the SIMPLE algorithm with collocated-variables arrangement is used to calculate the pressure and the velocities. More details of the pressure–velocity coupling algorithm can be found in [26].

The set of equations has been discretized by a finite-volume–finite-difference based method. The system of linear equations is solved by using Stone's strongly implicit

procedure (SIP). The time derivatives are discretized by a three-time-level scheme. The convection terms are discretized by a central difference second order scheme with deferred correction (CDS).

Time marching with fixed time step was used. The maximal number of outer iterations per time step was equal to 2000 allowing us to reach residuals of less than 10^{-3} for energy equation and less than 10^{-6} for momentum equations. We note that momentum conservation equations converge faster than energy equation. Namely when the residual of the energy equation reaches the value of 10^{-3}, the residual of momentum equations is less than 10^{-6}. To explain the difference in both residuals it must be noted, that we solve the conservation equations written in the dimensional form. Thus we have different residuals for energy and momentum equations due to different orders of magnitude of enthalpy and velocity. Numerical simulations with residual less than 10^{-4} for the energy equation showed identical cooling curves and velocity distributions. Several grid-convergence and time-step-convergence tests were performed to define proper grids and time steps leading to grid and time-step independent solutions. Details on time steps and grid resolutions used in the simulations are given in Table 1.

The validation of the solidification model and coupling algorithms was done in work [27]. It was shown that for $B < 1$ mT the experimental and numerical cooling curves at the axis of rotation and at different heights from the bottom of the mold agree reasonably well. The maximum deviations of 5 °C for $B = 0$ mT and 10 °C $B = 1$ mT were observed which can be explained by uncertainties in ε_{cr} definition and temperature dependency of transport properties. With increase of B the deviation between experimental and numerical temperatures increased. But at the same time the relatively good agreement in measured and calculated velocities was observed [27]. The reason of temperature deviation is under investigation.

3. Results

3.1. General remarks

Let us briefly recall the main findings of the isothermal RMF-driven acceleration of a liquid from a stable state of rest (spin-up) to provide a sound basis for the following sections. After switching on the RMF the first phase is an *initial adjustment* during which the inviscid fluid begins to rotate due to the externally imposed azimuthal acceleration. In parallel a meridional flow is induced by the unbalanced centrifugal forces. This occurs during approximately the first revolution about the axis. In the subsequently following *inertial* phase, the spin-up flow is dominated by an axially independent swirl in the core and Bödewadt layers on the rigid horizontal boundaries. This is accompanied by inertial oscillations. The development of the swirl occurs on the spin-up time scale given by [28,7,6]

$$t_{\text{spin-up}} = \frac{H_0}{\sqrt{\nu \Omega_{ce}}}. \tag{14}$$

The characteristic spin-up time for the various Ta numbers studied are summarized in Table 1. It decreases with increasing Ta. The effective rotation velocity Ω_{ce} of the inviscid core is then given by [6]:

$$\Omega_{ce} = \eta^{4/3}\left[\left(\frac{1}{4c}\right)^{2/3}\Omega_f\left(\frac{\Omega_f H_0^2}{\nu}\right)^{1/3}\right], \tag{15}$$

where c stands for the Bödewadt layer coefficient which is approximately $c = 1.35$. The parameter η describes the axial efficiency of the Lorentz force and depends strongly on the ratio H_0/R_0. For long and tall cylindrical molds ($H_0 \gg R_0$) η converges to unity. For wide molds of small height, however, η is small [6]. For the geometry used in this study ($H_0/R_0 = 2.5$) implying an aspect ratio of $A = 0.79$, the Lorentz force efficiency is moderately high ($\eta = 0.71$).

On increasing the Taylor number beyond a critical value [14] depending on the aspect ratio, large-scale oscillations occur [7]. These oscillations are caused by Taylor–Görtler (T–G) vortices which appear pairwise near the cylinder wall in between the two toroidal vortices of the secondary flow. These T–G vortices move towards top and bottom where they dissipate. Further increase of Ta causes a more and more random appearance of the T–G vortices possessing a complex three-dimension structure [29].

3.2. Description of the flow phases

With this picture in mind let us now combine this RMF-driven flow with the directional solidification. When bottom cooling of the melt coincides with switching on the RMF we are faced with two counteracting processes. The acceleration of the liquid phase during the *spin-up* is hindered by the progressive *solidification* which is accompanied by a decrease of the volume of the liquid phase, and consequently a modification of aspect ratio and forcing. To study these processes we make use of global velocities of the entire fluid in the cavity, which allow a transparent and elegant description of the complex and time-dependent behavior. Namely, we introduce the volume-averaged primary and secondary flow velocities, U_θ and U_{rz} as follows:

$$U_\theta = \frac{2}{R_0^2 H_0}\int_0^{H_0}\int_0^{R_0} r u_\theta \,\mathrm{d}r\,\mathrm{d}z, \tag{16}$$

$$U_{rz} = \frac{2}{R_0^2 H_0}\int_0^{H_0}\int_0^{R_0} r\sqrt{u_r^2 + u_z^2}\,\mathrm{d}r\,\mathrm{d}z. \tag{17}$$

In Fig. 2 we depict the time history of the volume-averaged angular velocity, Ω_{vol},

$$\Omega_{vol} = \frac{2}{R_0^2 H_0}\int_0^{H_0}\int_0^{R_0} u_\theta \,\mathrm{d}r\,\mathrm{d}z, \tag{18}$$

scaled with Ω_{ce}. For comparison we also show Ω_{vol} calculated for the isothermal spin-up. It can be seen that the

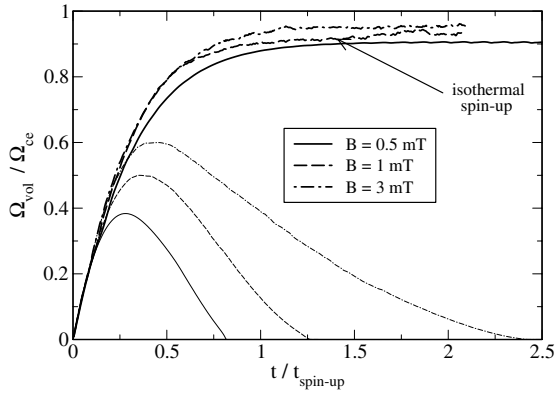

Fig. 2. Comparison of the time histories of $\Omega_{vol}/\ \Omega_{ce}$ calculated for the isothermal spin-up and solidification case.

solidification retards the melt convection since the angular velocity remains significantly smaller as compared to the isothermal melt.

To analyze the primary and secondary flow dynamics for different B we show in Fig. 3a and b the time histories of the volume-averaged azimuthal and meridional velocities, U_θ and U_{rz}. To compare the meridional velocity, responsible for the convective transport towards the solidification front, with the velocity of the solidification front

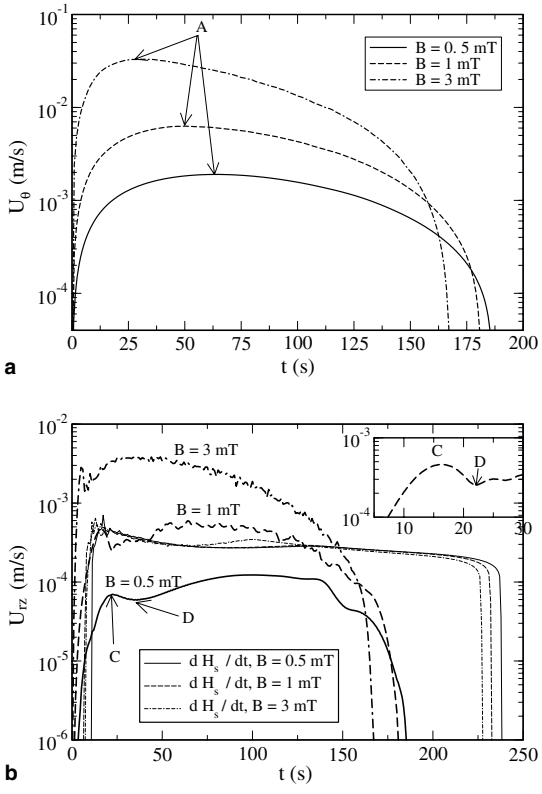

Fig. 3. Time history of U_θ during solidification (a); the time history of U_{rz} (b). The capital letters, C, D and A, refer to either the end of the *initial adjustment phase*, the first minimum of U_{rz} or the start of the *braking* phase. For comparison the velocity of the solidification front, dH_s/dt, is inserted (fine lines) in (b).

itself we additionally plot in Fig. 3b the volume-averaged velocity of the solid front, $\partial H_s/\partial t$, where H_s is given by

$$H_s = \frac{2}{R_0^2}\int_0^{H_0}\int_0^{R_0} \varepsilon_s r\,dr\,dz. \tag{19}$$

This formulation for H_s was chosen since it is able to handle the non-planarity of the solidification front at higher Ta numbers as shown later on. For the cooling rate chosen the velocity of the solidification front is 0.2–0.3 mm/s. It can be seen that for $B \geqslant 1$ mT the meridional velocity exceeds the velocity of the solid front. The resulting impact of U_{rz} on the shape of the mushy zone is discussed later on.

The analysis of Fig. 3a and b shows three different phases of the flow during UDS. On referring to the isothermal spin-up [6] we denote them as

(1) *initial adjustment (i.a.)* phase;
(2) *inertial* or *non-linear* phase;
(3) *braking* phase.

The first *initial adjustment (i.a.)* phase comprises the temporal interval from zero until point C (Fig. 3b) which is localized at approximately $0.1 \cdot t_{spin\text{-}up}$. This phase is completed upon achieving the first maximum in the volume-averaged kinetic energy of the secondary flow. The flow pattern of this phase has the shape of two toroidal vortices located symmetrically with respect to the midplane of the cylinder, see Fig. 4b. The suppression of the lower vortex at smaller Ta numbers (Fig. 4a) is caused by buoyancy as shown in Section 3.3. Due to the short stage of the *i.a.* phase the viscous effects play a minor role.

The second *inertial* or *non-linear* phase [7,6] is located between the first local maximum of U_{rz} (point C, Fig. 3b) and the maximum of U_θ (point A), Fig. 3a). This regime is basically characterized by a non-linear increase of volume-averaged azimuthal velocity, U_θ. We found that, similar to the isothermal case [7,6], the first local minimum in the time history of U_{rz} (point D) belongs to the formation of the Bödewadt layer on the liquid–solid boundary. The corresponding snapshots for two different B are presented in the Fig. 5. The flow reversal leading to the characteristic spatially oscillating structure of the Bödewadt layer is clearly visible in Fig. 5b. A main feature of the *inertial* phase are inertial oscillations in the meridional flow between the flow structure belonging to points C and D. The way how the flow structure is transformed resembles closely the isothermal case [7,6]. A marked consequence of the inertial oscillations are fluctuations in the cooling curves which are suppressed under normal g but visible for $g = 0$ (cf. Section 3.3). Increase of magnetic field induction B, respectively Ta number beyond $Ta > 5.1 \times 10^4$, forces the appearance of Taylor–Görtler vortices already during the inertial phase.

The third, *braking* phase starts at point A (Fig. 3a), which belongs to $t \approx 0.35 \cdot t_{spin\text{-}up}$, which is valid as long as the solidification time is of the same order of magnitude

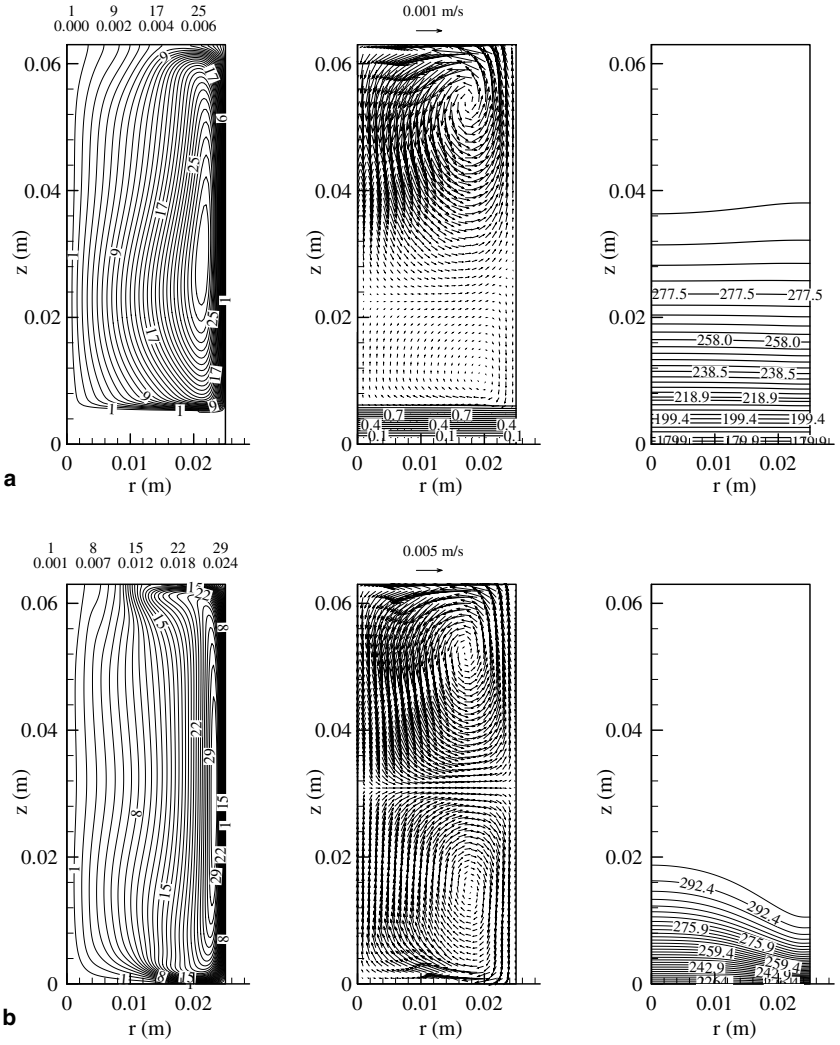

Fig. 4. Azimuthal velocity contours (left), meridional velocity vectors plus liquid isolines (middle) and isotherms (right) at the end of the *initial adjustment phase* at $t \sim 0.1 \cdot t_{\text{spin-up}}$ (point C) corresponding to the first local maximum in the history of U_{rz} in Fig. 3b. (a) $B = 1$ mT, (b) $B = 3$ mT.

as $t_{\text{spin-up}}$. This phase is characterized by a decrease of the absolute value of volume-averaged azimuthal velocity. Fig. 6 depicts a snapshot of the flow and the temperature distributions at the time corresponding to the global maximum of U_θ located at point A in Fig. 3a. The braking of the primary flow occurs for all magnetic field strengths studied and is noticeable when approximately one third of the melt is solidified. For $B > 0.5$ mT this phase is characterized by randomly appearing Taylor–Görtler vortices moving up and downward along the side wall of the cylinder. Nevertheless, the meridional flow, averaged over three rotations of the liquid melt, consists of two big toroidal vortices (Fig. 7) where the meridional velocity in the upper vortex near the free surface is about two times larger than that of the lower vortex near the mushy zone (e.g. for $B = 3$ mT the maximal meridional velocities in the upper and lower vortices are about 7 mm/s and 3 mm/s, respectively). Fig. 7 shows that the mean-time pattern of the primary flow in the interval $[0; R_0/\sqrt{2}]$ corresponds to a rigid body rotation. The remaining interval $[R_0/\sqrt{2}; R_0]$ until the wall is the zone where the T–G vortices appear, which is in close agreement with the work of Kaiser and Benz [8]. At $r \sim R_0/\sqrt{2}$, the azimuthal velocity reaches its maximum.

Let us now study the impact of the secondary flow governing the advection of heat and mass to or away from the mushy zone. On the axis of rotation where the secondary flow is directed upwards, the heat transfer from the solidification front is enhanced. Close to the lateral walls the secondary flow is directed towards the mushy zone thus the temperature gradient at this place is increased in comparison to the gradient on the axis of rotation. As a result a convex curvature of the solid front sets in which is clearly visible in Fig. 8. This marked effect of the secondary flow occurs as soon as the volume-averaged meridional velocity exceeds the volume-averaged velocity of solid front, i.e. when $U_{rz} > \frac{\partial H_{es}}{\partial t}$. In our parameter range this is the case for $B \geqslant 1$ mT (cf. Fig. 3b). Within the secondary flow the T–G vortices are an important ingredient since they are a further mechanism for the enhancement of heat and mass transfer. The T–G vortices are advected by meridional flow

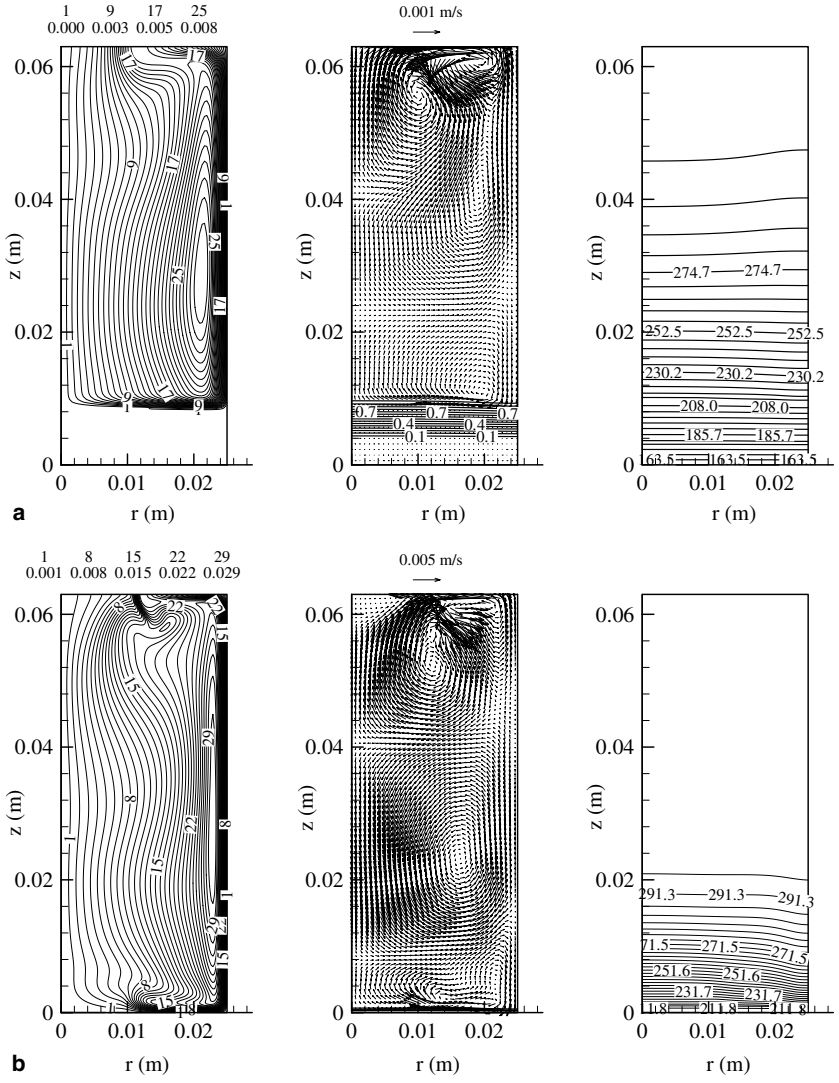

Fig. 5. Azimuthal velocity contours (left), meridional velocity vectors plus liquid isolines (middle) and isotherms (right) at $t \sim 0.15 \cdot t_{\text{spin-up}}$ (point D) corresponding to the first local minimum in the history of U_{rz} in Fig. 3b. (a) $B = 1$ mT, (b) $B = 3$ mT.

towards the free surface and the mushy zone where they are dissipated. This dissipation is the origin of thermal waves imposing a wavy roughness onto the mushy zone (cf. Fig. 8), which was observed experimentally by Eckert et al. [27]. The nature of the thermal waves is the fluctuations of the enthalpy caused by fluid flow oscillations in the slurry region due to dissipation of T–G vortices. In this way these fluctuations lead to the oscillations of the volume fraction of liquid and the temperature. To ensure the absence of the influence of numerical "waves" first, we performed grid study similar to the one done by Nikrityuk et al, see Fig. 4 in Ref. [6]. Namely the grid we use in simulations gives the grid independent solution. Second we use smoothed (exponential) dependency of the molecular viscosity in the slurry region, $\varepsilon > \varepsilon_{\text{cr}}$, on the volume fraction of liquid, see Eq. (5), to avoid the appearing of numerical instabilities in the upper mushy zone. We suppose that the thermal waves may produce a local remelting of dendrites. At the same time the local remelting of dendrite arms may produce local enrichment by Sn of the liquid phase in the mushy zone. In the case of columnar dendrites in the mushy zone all these effects may cause columnar-equiaxed transition (CET).

Next we want to show the influence of the *Ta* number on the cooling curves. Fig. 9 shows cooling curves obtained at the positions $z = 2.0$ cm and 5.5 cm for different *Ta* numbers. The tendency of increasing cooling on the axis of rotation with increase of *Ta* can be seen. This is in good agreement with the experimental data [4]. The difference between $B = 0$ and 1 mT is not significant. However, for $B = 3$ mT the deviation is increased. The secondary flow induced by Ekman pumping increases the heat transfer coefficient at the mushy zone. Near the wall we have the inverse process: the downward flow decreases the cooling rate, $\partial T/\partial t$, in comparison to that on the axis of rotation.

3.3. Impact of buoyancy

To understand the impact of gravity on the flow pattern of Section 3.2 and the macrosegregations (Section 3.4) a

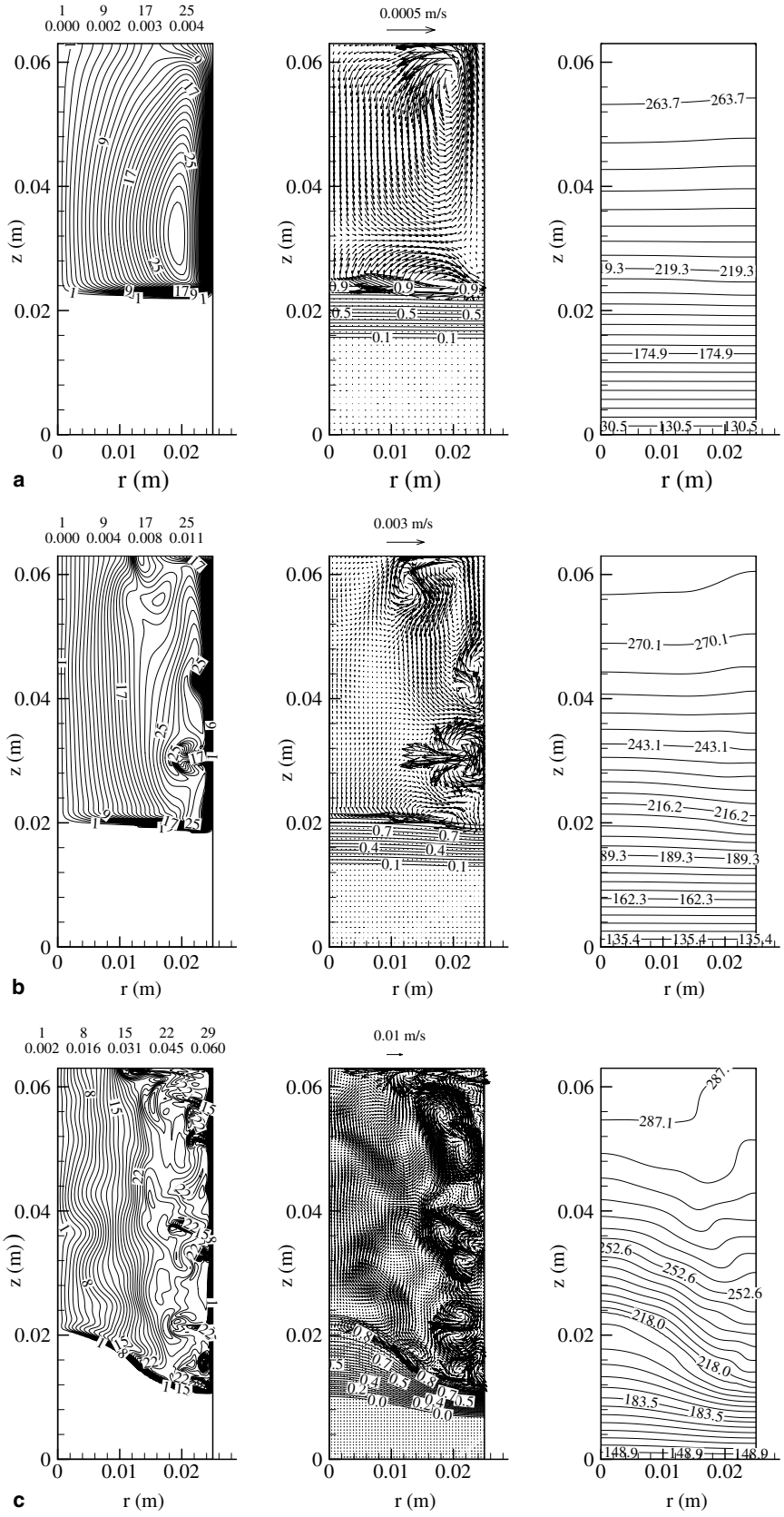

Fig. 6. Azimuthal velocity contours (left), meridional velocity vectors plus liquid isolines (middle) and isotherms (right) at $t \sim 0.35 \cdot t_{\text{spin-up}}$ (point A) corresponding to the global maximum in the history of U_θ in Fig. 3a. (a) $B = 0.5$ mT, (b) $B = 1$ mT, (c) $B = 3$ mT.

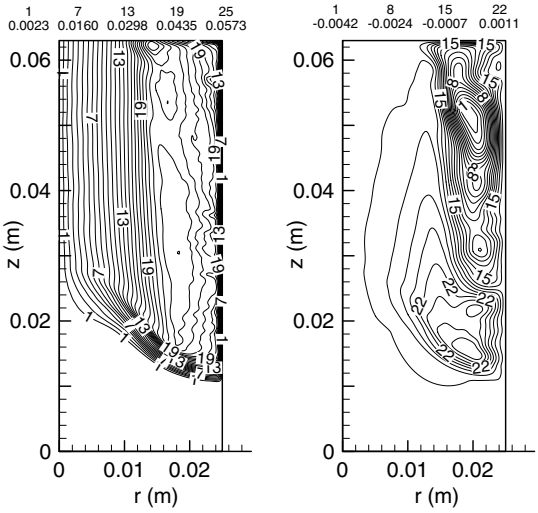

Fig. 7. The flow pattern for $B = 3$ mT averaged over three rotations in the time interval $33\text{ s} \leqslant t \leqslant 45\text{ s}$. Azimuthal velocity (left) and meridional velocity (right).

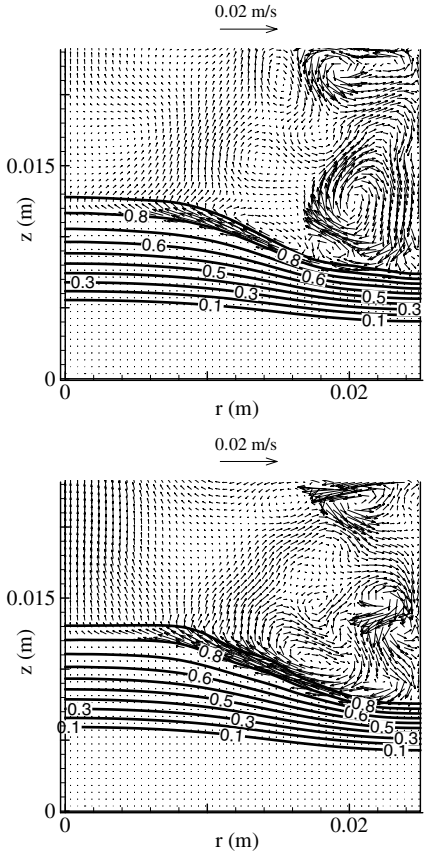

Fig. 8. Modification of the shape of the mushy zone (black lines corresponds to the isovolumes of liquid fraction) caused by the meridional flow for $t = 23.24$ s (up) and 24.00 s (down). $B = 3$ mT.

number of simulations with $g = 0$ were performed. We observe that the time histories of U_θ stay very close to that detected under terrestrial conditions (Fig. 3a). By contrast, significant changes in the behavior of U_{rz} occur which are

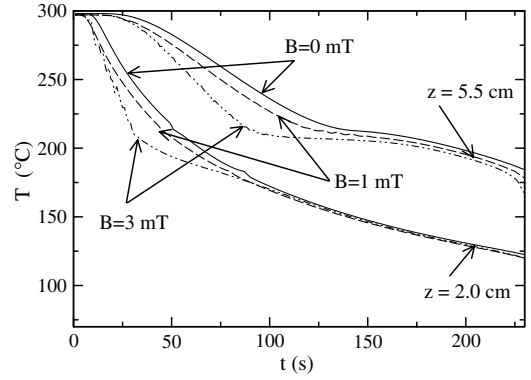

Fig. 9. Comparison of the cooling curves for different Ta. $T_0 = 293$ °C.

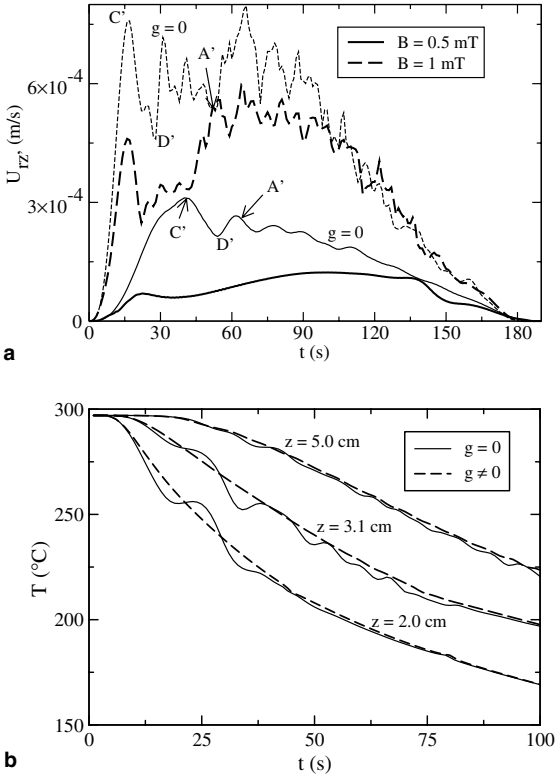

Fig. 10. The influence of buoyancy force: (a) the time history of U_{rz} calculated with $g = 0$ for $B = 0.5$ mT and 1 mT. For comparison the corresponding curves with $g \neq 0$ are inserted. The primed capital letters are the "microgravity analogue" to the non-primed quantities in Section 3.2, (b) comparison of the cooling curves calculated with (dashed line) and without (solid line) buoyancy force for $B = 1$ mT.

shown in Fig. 10a for $B = 0.5$ mT and 1 mT. For $B = 3$ mT the time histories of U_{rz}, obtained for $g = 0$ and $g \neq 0$, are again nearly identical. It can be seen that the maximum damping of the convection occurs during the *initial adjustment* (between $t = 0$ and point C′) and *inertial* (between the points C′ and A′) phases which is caused by the high temperature gradients existing during the beginning of solidification.

Inspecting the flow dynamics under microgravity, we observed a much more distinct double vortex structure in which the intensities of both vortices are comparable. Thus the suppression of the lower vortex under normal gravity, see Fig. 4b, is indeed due to the stable density stratification at the beginning which dissipates a part of the kinetic energy available under microgravity. As a result, under normal g the temperature isotherms have a planar shape, see Fig. 4a and b. The flow dynamics and the heat transfer during the *braking* phase are not different from the gravity presence case described above.

On comparing the volume-averaged meridional flow velocities under normal and microgravity (Fig. 10a) we find under microgravity an increase of the velocity by approximately a factor of two. Thus, under microgravity already the lowest $B = 0.5$ mT studied is sufficient to achieve the same velocity as the solidification front, dH_s/dt (cf. Fig. 3b). As a result, the impact of the meridional flow onto the shape of the mushy zone is considerably stronger under microgravity.

Numerical simulations with and without solutal buoyancy in all cases showed the same time histories of U_θ and U_{rz}. Thus the solutal buoyancy is small in comparison to thermal buoyancy. A threshold beyond which the buoyancy influence can be neglected is derived in Section 4.

Fig. 10b depicts the consequences of microgravity on the time history of the temperature. It shows persistent temperature oscillations, the amplitude of which depends on the height of the thermoelement position. The period of these oscillations decreases with time and reaches a value of approximately 7 s for the upper thermoelement. These oscillations are caused by the inertial waves existing during RMF-driven spin-up [6].

3.4. Macrosegregations

The simulations with the assumption $\vec{u}_s = \vec{u}_l$ ($S_h = 0$, $S_c = 0$) showed no macrosegregations. This is a natural consequence of the vanishing source term $S_c = 0$ in Eq. (8). The remaining diffusive term $\nabla\rho_m D\nabla(C_l - C)$ is not able to provoke macrosegregation due to the disparate macrotime scales for diffusion, $O(10^3\ s)$, and solidification, $O(10^2\ s)$, at the given solidification rates of 0.2–0.3 mm/s. However, it is a well known fact that the solidification process which takes place with strong fluid flow normally produces significant segregations. Unfortunately we did not find in the literature an extra relationship between $\vec{u}_s$ and $\vec{u}_l$ for rotating melt for the mixture continuum model. The usage of a model developed by Ni and Incropera [15] which describes the relations for solid and liquid velocities under gravity condition showed a solute distribution that contradicts the experimental data for RMF-driven solidification [3]. To overcome this problem we introduce a linear relation between $\vec{u}_s$ and $\vec{u}$ by analog to linear model of Flood et al. [30], which is based on the assumption that the velocity of free floating dendrites is proportional to the fluid flow velocity in the slurry region of the mushy zone, namely:

$$\vec{u}_s = \sqrt{\varepsilon}\vec{u}. \tag{20}$$

We note that this concept lacks a physical basis and can be used only for qualitative [31] analysis of an impact of the movement of the equiaxed dendrites on the macrosegregation. Surprisingly we found that Eq. (20) works well. For $Ta < 10^6$ this model produces segregation rates of less than <2% in accord with the experiments [4]. Furthermore, this sort of computed segregations correlates well with the data of Roplekar and Dantzing [3] as explained next. Fig. 11 displays the computed distribution of the mixture mass concentration of Sn normalized with $C_0 = 0.85$ after complete solidification at $t = 220$ s ($B = 1$ mT). Roplekar and

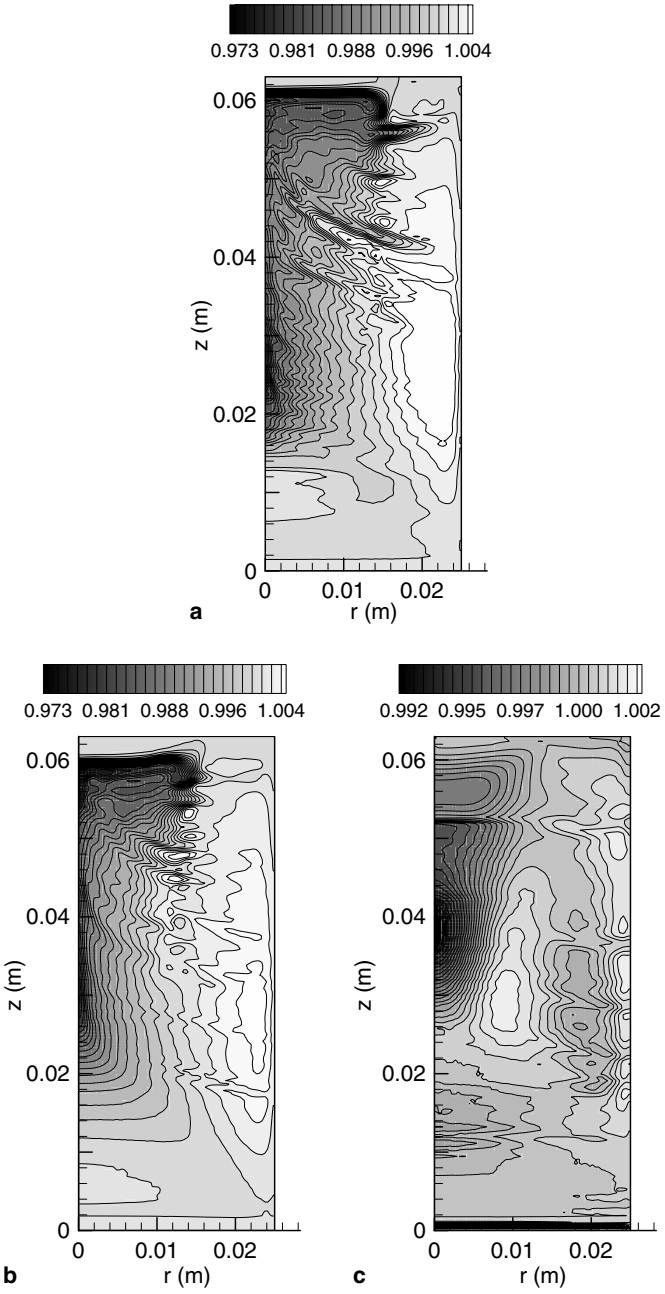

Fig. 11. Predicted macrosegregations for $B = 1$ mT at $t = 220$ s. (a) $g = 0$, (b) $g \neq 0$, $\beta_S = 0$, (c) $g \neq 0$, $\beta_S = 0.2$.

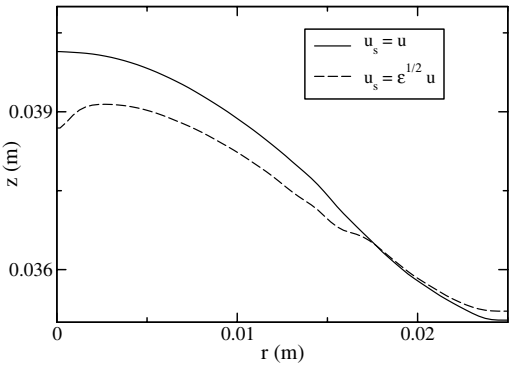

Fig. 12. Predicted shape of the mushy zone corresponding to $\varepsilon = 0.99$ for $B = 1$ mT at $t = 100$ s. $\beta_S = 0$.

Dantzig [3] showed that the application of an RMF leads to macrosegregations in radial and axial direction. In particular, an enrichment of the eutectic phase was found on top and in the central region of the cylinder. This finding is confirmed by our results (Fig. 11) showing a negative segregation on the axis of rotation and on the top of the cylinder. This phenomenon is attributed to the secondary flow inside the liquid phase. The vortex near the mushy zone carries liquid which is rejected ahead of the mushy zone towards the middle of the liquid phase. This liquid is depleted in Sn since the liquid concentration continuously decreases along the liquidus line until the eutectic concentration is reached. In particular, the advection of liquid depleted in the lighter component is responsible for the development of a liquid channel on the axis of rotation inside of the mushy zone at a slow cooling rate, as predicted by Hainke et al. [9]. Fig. 12 illustrates this effect for our system. The shifting of mixture concentration toward the eutectic concentration on the axis of rotation causes an M-shaped profile of the mushy zone.

The result of simulations showed furthermore that the macrosegregations under microgravity are even worse than under terrestrial conditions, see Fig. 11. In particular, the oscillations caused by inertial waves under microgravity lead to isoconcentration lines which spatially oscillate along the z-axis in the lower part of the cavity, see Fig. 11a. Under normal gravity (cf. Fig. 11c) the macrosegregations are less distinct since the secondary flow is damped by the stable density stratification provided that $Ta < 1.7 \times 10^6$.

4. Discussion

Generally the solidification of a metal alloy is characterized by the existence of the jump of the electric conductivity at the liquid/mold and liquid/solidification front. To reduce the computational costs we restrict this work to the assumption $\sigma_s/\sigma_l = 1$ in order to be able to investigate the interference of spin-up problem with the solidification of the melt in more detail. But we note that in general case it is necessary to couple the calculation of conservation equations with Lorentz force calculation [32]. Simplified simulations showed that e.g. for the ratio $\sigma_s/\sigma_l = 5$ the volume-averaged azimuthal and meridional velocities exceed their values calculated for $\sigma_s/\sigma_l = 1$ at about 15% [32]. The numerical study of the influence of the ratios σ_s/σ_l and σ_w/σ_l on the fluid flow induced by RMF during solidification of PbSn alloy is on progress and will be published elsewhere.

Let us now turn to the rather specific influence of buoyancy on the flow pattern which is pronounced at lower Ta number while it is no longer significant for $Ta \sim 1.8 \times 10^6$ (3 mT). To derive a more precise criterion we consider the instant when the centrifugal force exceeds the buoyancy force, namely:

$$u_\theta^2/r > g(\beta_T(T_s - T_{ref}) + \beta_C(C_s - C_{ref})). \tag{21}$$

In the case that solutal buoyancy is smaller than thermal buoyancy, after some transformations, using $\Omega = u_\theta/r$ we obtain

$$E < \sqrt{1/Gr}. \tag{22}$$

Here E and Gr are Ekman and Grashof numbers, respectively:

$$E = \frac{\nu}{\Omega R_0^2}, \quad Gr = \frac{gR_0^3\beta_T(T_s - T_{ref})}{\nu^2}. \tag{23}$$

Eq. (22) was used implicitly in work [33], where it was shown, using the Richardson number, $Ri = GrE^2$, that in a rotating fluid buoyancy has a major influence on the meridional flow provided $Ri \geqslant 1$. In our case using the magnetic Taylor number and Eqs. (15), (22) and (23) we obtain:

$$Ta > \frac{c}{A^2\eta^2} Gr^{3/4}, \tag{24}$$

where $A = 2R_0/H_0$ and η depends on A. Following Eq. (24), thermal buoyancy can be neglected for $Ta > 1.7 \times 10^6$ corresponding to $B > 2.9$ mT. This is in close agreement with our numerical results.

Despite the advantages of the present mixture viscosity model in treating the fluid dynamic aspects of solidification there exist some limitations which we briefly want to address (for a more detailed discussion we refer to [34]). In our simulation ε_{cr} is the key uncertainty which has an influence on the calculated temperature. A more closer inspection shows that shifting ε_{cr} from 0.8 to 0.5 enhances the heat transfer by approximately 10%. This is due to a "liquidisation" of the upper mushy zone resulting in a faster cooling of the melt. In the general case the value of ε_{cr} should depend on the cooling rate. A significant improvement foreseen in future work is to relate ε_{cr} to the local undercooling determining the thickness of the slurry region in the mushy zone.

5. Summary

In this paper we analyze the directional solidification of Pb85wt%Sn in presence of a forced convection. This

convection is driven by a rotating magnetic field (RMF) with Taylor numbers, Ta, up to $Ta = 2 \times 10^6$. In particular we study the case when the beginning solidification interferes with the so-called spin-up of the hot melt. Based on the analysis of the time histories of the volume-averaged azimuthal and meridional velocities, the RMF-driven flow can be divided into three phases, which are passed through as time goes by. The first two phases, *inertial adjustment (i.a.)* and *inertial* phase are similar to the isothermal spin-up problem [7,6]. The third, *braking* phase is characterized by a decrease of global azimuthal velocity U_θ mainly due to the permanent decrease of the volume of the liquid fraction which implies an increase of the aspect ratio $(2R_0/H_l)$ of the melt. In this way the braking torques arising from friction in the Bödewadt and side wall layers retard increasingly the flow in the melt.

The influence of the meridional flow on the shape of the mushy zone becomes noticeable as soon as the meridional velocity U_{rz} exceeds the volume-averaged velocity of solid front $\partial H_s/\partial t$. For our cooling rate this occurs at $Ta \sim 2 \times 10^5$. From this instant on, the secondary flow is responsible for a variety of effects. First, it enhances the heat transfer coefficient at the mush-liquid boundary and thereby provoking the marked change in slope of the cooling curves visible on increasing Ta. Second, due to the transport of hot melt towards the mush zone in regions close to the lateral walls, a slower growth of the mushy zone occurs there leading to the convex shape of the latter. With increase of Ta, Taylor–Görtler (T–G) vortices appear along the side wall which further enhance the heat and mass transport due to their advection with the secondary flow. Dissipation of T–G vortices in the mushy zone causes thermal waves in the upper part of the mushy zone imposing a wavy substructure on it.

Due to the initially stable density stratification in the hypereutectic PbSn-alloy, buoyancy plays an important role at low Ta. Buoyancy drastically damps the lower meridional flow vortex, close to the mushy zone, thereby significantly reducing the impact of the RMF-driven flow on solidification. For $Ta \geqslant 10^6$ and $A = 0.79$ the buoyancy influence can be neglected as derived in Section 4.

Acknowledgments

The authors are grateful to Dr. M. Peric for the source code of the 2D pressure–velocity solver. We thank Dr. S. Eckert and B. Willers for sharing their experimental data. The authors are also grateful to Dr. Ying Shi for critical reading of the manuscript. Financial support by the Deutsche Forschungsgemeinschaft (SFB 609) is gratefully acknowledged.

References

[1] A.A. Tsavaras, H.D. Brody, Electromagnetic stirring and continuous casting-achievements, problems and goals, J. Met. 167 (1984) 31–37.

[2] P.A. Davidson, An Introduction to Magnetohydrodynamics, Cambridge University Press, Cambridge, 2001.

[3] J.K. Roplekar, J.A. Dantzing, A study of solidification with a rotating magnetic field, Int. J. Cast Met. Res. 14 (2001) 79–98.

[4] B. Willers, S. Eckert, U. Michel, G. Zouhar, Effect of the fluid convection driven by a rotating magnetic field on the solidification of a PbSn alloy, in: D.M. Herlach (Ed.), Solidification and Crystallization, Wiley-VCH Verlag GmbH & Co. KGaA, Weinheim, 2004.

[5] B. Willers, S. Eckert, U. Michel, I. Haase, G. Zouhar, The columnar-to-equiaxed transition in Pb–Sn alloys affected by electromagnetically driven convection, Mater. Sci. Eng. A 402 (2005) 55–65.

[6] P.A. Nikrityuk, M. Ungarish, K. Eckert, R. Grundmann, Spin-up of a liquid metal flow driven by a rotating magnetic field in a finite cylinder. A numerical and analytical study, Phys. Fluids 17 (2005) 067101.

[7] P.A. Nikrityuk, K. Eckert, R. Grundmann, Numerical study of spin-up dynamics of a liquid metal stirred by rotating magnetic fields in a cylinder with the upper free surface, Magnetohydrodyn. J. 40 (2004) 127–146.

[8] Th. Kaiser, K.W. Benz, Taylor vortex instabilities induced by a rotating magnetic field: a numerical approach, Phys. Fluids 10 (5) (1998) 1104–1110.

[9] M. Hainke, J. Friedrich, G. Müller, Numerical study on directional solidification of AlSi alloys with rotating magnetic fields under microgravity conditions, J. Mater. Sci. 39 (2004) 2011–2015.

[10] S. Eckert, B. Willers, G. Gerbeth, Measurements of the bulk velocity during solidification of metallic alloys, Metall. Mater. Trans. A 36A (2004) 267–270.

[11] W.D. Bennon, F.P. Incropera, A continuum model for momentum, heat and species transport in binary solid–liquid phase change systems I. Model formulation, Int. J. Heat Mass Transfer 30 (10) (1987) 2161–2170.

[12] L. Martin Witkowski, J.S. Walker, Nonaxisymmetric flow in a finite-length cylinder with a rotating magnetic field, Phys. Fluids 11 (1999) 1821–1826.

[13] J. Priede, Yu.M. Gelfgat, Mathematical model of the mean electromagnetic forces induced by a rotating magnetic field in a liquid column of a finite length, Magnetohydrodynamics 32 (1996) 249–256.

[14] I. Grants, G. Gerbeth, Stability of axially symmetric flow driven by a rotating magnetic field in a cylindrical cavity, J. Fluid Mech. 431 (2001) 407–426.

[15] J. Ni, F.P. Incropera, Extension of the continuum model for transport phenomena occurring during metal alloy solidification—II. The microscopic considerations, Int. J. Heat Mass Transfer 38 (7) (1995) 1285–1296.

[16] B.J. Yang, D.M. Stefanescu, J. Leon-Torres, Modelling of microstructural evolution with tracking of equiaxed grain movement for multicomponent Al–Si alloy, Metall. Mater. Trans. A 32A (2001) 3065–3076.

[17] A. Kumar, P. Dutta, Modeling of transport phenomena in continuous casting of non-dendritic billets, Int. J. Heat Mass Transfer 48 (2005) 3674–3688.

[18] The Goodfellow website: www.goodfellow.com. Metals, polymers, ceramics and other materials.

[19] Verein Deutscher Ingenieure (VDI)-Wärmeatlas Berechnungsblätter für den Wärmeübergang, 9 Auflage, Springer-Verlag, Berlin, 2002.

[20] D.R. Poirier, Densities of PbSn alloys during solidification, Metall. Trans. A 19A (1988) 2349–2354.

[21] P.J. Prescott, F.P. Incropera, Magnetically damped convection during solidification of a binary metal alloy, J. Heat Transfer 115 (1993) 302–310.

[22] Th.B. Massalski (Editor-in-chief), Binary Alloy Phase Diagrams, vol. 3, second ed., ASM International, Materials Park, OH 44073, USA, 1990.

[23] C.R. Swaminathan, V.R. Voller, Towards a general numerical scheme for solidification systems, Int. J. Heat Mass Transfer 40 (1997) 2859–2868.

[24] A. Spohn, M. Mory, E.J. Hopfinger, Observation of vortex breakdown in an open cylindrical container with a rotating bottom, Exp. Fluids 14 (1993) 70–77.
[25] P. Dold, K.W. Benz, Rotating magnetic fields: fluid flow and crystal growth applications, Progr. Cryst. Growth Characterisation Mater. 38 (1999) 7–38.
[26] J.H. Ferziger, M. Peric, Computational Methods for Fluid Dynamics, third ed., Springer-Verlag, 2002.
[27] S. Eckert, B. Willers, P.A. Nikrityuk, K. Eckert, U. Michel, G. Zouhar, Application of a rotating magnetic field during directional solidification of Pb–Sn alloys: consequences on the CET, Mater. Sci. Eng. A, in press.
[28] M. Ungarish, The spin-up of liquid metal driven by a rotating magnetic field, J. Fluid Mech. 347 (1997) 105–118.
[29] J. Stiller, K. Frana, R. Grundmann, U. Fladrich, W. Nagel, A parallel PSPG finite element method for direct simulation of incompressible flow, in: M. Danelutto et al. (Eds.), Proceedings of the 10th International Euro-Par Conference, Springer-Verlag, Berlin, 2004, pp. 726–733.
[30] S.C. Flood, L. Katgerman, V.R. Voller, The calculation of macrosegregation and heat and fluid flow in the D.C. casting of aluminum alloys, in: M. Rappaz et al. (Eds.), Modeling of Casting, Welding and Advanced Solidification Processes V, TMS, Warrendale, PA, 1991, pp. 683–690.
[31] Strictly speaking the generalization $\vec{u}_s \neq \vec{u}$ requires the incorporation of a source term in Eq. (3) describing the momentum transfer between solid and liquid phases similar to the Blake–Kozeny relation. This term is neglected for the present study.
[32] P.A. Nikrityuk, K. Eckert, R. Grundmann, Rotating magnetic field driven flows in conductive inhomogeneous media. Part. I: Numerical study, Metall. Mater. Trans. B, accepted for publication.
[33] R. Iwatsu, Flow pattern and heat transfer of swirling flows in cylindrical container with rotating top and stable temperature gradient, Int. J. Heat Mass Transfer 47 (2004) 2755–2767.
[34] C. Beckermann, C.Y. Wang, Multiphase/-scale modeling of alloy solidification, Ann. Rev. Heat Transfer 6 (1995) 115–198.